

A Study of Nine High-Redshift Clusters of Galaxies : I. The Survey

J. B. Oke

Palomar Observatory, California Institute of Technology, Pasadena, CA 91125

and

Dominion Astrophysical Observatory, 5071 W. Saanich Road, Victoria, BC V8X 4M6

Electronic mail: oke@dao.nrc.ca

Marc Postman

Space Telescope Science Institute¹, 3700 San Martin Drive, Baltimore, MD 21218

Electronic mail: postman@stsci.edu

Lori M. Lubin^{2,3}

Observatories of the Carnegie Institution of Washington, 813 Santa Barbara Street
Pasadena, CA 91101

Electronic mail: lml@astro.caltech.edu

Accepted for publication in the *Astronomical Journal*

ABSTRACT

We present a description of the observations and data reduction procedures for an extensive spectroscopic and multi-band photometric study of nine high redshift, optically-selected cluster candidates. The primary goal of the survey is to establish new constraints on cluster and galaxy evolution, with specific emphasis on the evolution of galaxy morphology and on the star-formation history of the galaxies within and around distant clusters. We have measured 892 new redshifts for galaxies with $R \leq 23.3$. The data will also serve as deep probes of the foreground and background large-scale structures. The observations include broad band optical imaging and spectroscopy with the Low Resolution Imaging Spectrograph at the 10 meter W. M. Keck Observatory telescope; K-band imaging with IRIM at the 4 meter Kitt Peak National Observatory telescope; and deep, high angular resolution imaging with the WFPC2 onboard the Hubble Space Telescope. We also describe the procedures used to obtain morphological information. We have established that six of the nine cluster candidates are indeed real space density enhancements and are representative of those typically associated with clusters of galaxies. The remaining three candidates appear to be projections of several smaller groups at widely separated distances. This success rate is consistent with estimates of the false positive rate in 2D optical high- z cluster searches.

Subject headings: galaxies : clusters of galaxies; galaxies : distances and redshifts; surveys

¹Space Telescope Science Institute is operated by the Association of Universities for Research in Astronomy, Inc., under contract to the National Aeronautics and Space Administration.

²Hubble Fellow

³Present Address : Palomar Observatory, California Institute of Technology, Mail Stop 105-24, Pasadena, CA 91125

1. Introduction

Clusters of galaxies have historically provided an important tool for studying cosmology and the evolution of galaxies. Because of their high concentration of galaxies, clusters provide an environment in which to study large, statistical samples of galaxies. Therefore, examining clusters of galaxies from the local universe to those at high redshift allows us to probe galactic evolution to redshifts of the order of 1. Clusters of galaxies at redshifts of $z \lesssim 0.2$ have been extremely well cataloged in the optical regime (e.g. Abell 1958; Zwicky *et al.* 1968; Dressler 1980; Shectman 1985; Abell *et al.* 1989; Lumsden *et al.* 1992; Dalton *et al.* 1994). The analyses of local clusters indicate that these systems are dense (Abell richnesses of $\sim 30 - 300$ galaxies), massive ($M \sim 10^{14} - 2 \times 10^{15} h^{-1} M_{\odot}$), and dominated by early-type galaxies ($\sim 50 - 80\%$ of the total galaxy population). These studies provide a strong basis on which to compare cluster properties at increasingly higher redshift.

Detailed photometric, spectroscopic and morphological studies have been extended to clusters of galaxies at redshifts up to $z \sim 0.6$. The first substantial contribution at these redshifts came from Butcher & Oemler (1984) who found a surprisingly large population of blue galaxies in conjunction with the expected red sequence of early-type cluster members. Further photometric and spectroscopic campaigns, including the ambitious CNOC and MORPHS surveys, have confirmed the progressive bluing of the cluster's galaxy population and have tracked the passive evolution of the early-type galaxies (Dressler & Gunn 1992; Oke, Gunn & Hoessel 1996; Yee, Ellingson & Carlberg 1996; Ellingson *et al.* 1997; Ellis *et al.* 1997; Stanford *et al.* 1995, 1997; and references therein). The Hubble Space Telescope (HST) has enabled morphological classification of intermediate-redshift ($z \lesssim 1$) galaxies on scales which are comparable to the classifications made of their local counterparts. These high-resolution studies have revealed that there may be a substantial change in the morphological composition of the clusters (Smail *et al.* 1997; Dressler *et al.* 1997; however, see Stanford *et al.* 1997). All of these results imply that there is a significant amount of evolution occurring in the cluster environment between redshifts of $z \approx 0.5$ and $z = 0.0$. In order to understand this apparent change in the galaxy population, it is essential to probe in similar detail clusters of galaxies at even higher redshift where the effects of evolution and cosmology will be even greater. In light of this, we have undertaken an extensive survey of nine candidate clusters of galaxies at redshifts greater than 0.6. Only a few optical/near-IR surveys have attempted to detect systematically clusters at high redshift; therefore, we have chosen our cluster sample from the Gunn, Hoessel, & Oke (1984) survey and the Palomar Distant Cluster Survey (Postman *et al.* 1996).

The observational data compiled for this survey, to date, includes deep *BVRIK* photometry, over 900 low-resolution spectra, and deep F606W/F702W/F814W imagery from HST. The large redshift database allows us to reliably distinguish between physically real clusters and chance line-of-sight projections. The full data allow us to measure the global properties of the clusters, such as profile shape and dynamics, as well as the individual properties of the cluster galaxies, such as color, star-formation rate, and morphology. In this introductory paper to our high-redshift cluster series, we describe in detail the observational and data reduction techniques of each aspect of this survey and present the redshift histograms for our nine fields. The subsequent papers in this series will present the specific analyses and scientific results of this survey. These papers include the second and third installments in this series which present a detailed photometric, spectroscopic, and morphological analyses of the first two clusters to be completed in this survey, CL0023+0423 and CL1604+4304 (Postman, Lubin & Oke 1998; Lubin *et al.* 1998).

2. The Cluster Sample

Over the past several years, clusters of galaxies at intermediate redshifts ($z \sim 0.5$) have been well-studied (e.g. Dressler & Gunn 1992; Dressler *et al.* 1994; Oke, Gunn & Hoessel 1996; Carlberg *et al.* 1997; Ellis *et al.* 1997; Smail *et al.* 1997). With the completion of the Keck Telescope and the Low Resolution Imaging Spectrometer (LRIS), the ability to obtain spectra of cluster galaxies at $z > 0.5$ became feasible with only modest allocations of observing time. Two catalogs of distant, northern cluster candidates were available, those of Gunn, Hoessel & Oke (1986) and Postman *et al.* (1996). Both surveys were based on six fields spread fairly uniformly around the sky. The present sample consists of nine candidate high-redshift clusters selected from these fields.

Seven of the nine clusters are from the catalog of Gunn, Hoessel & Oke (1986). All of these clusters were discovered on red (600-710 nm) or near-infrared (800 nm) images and had spectra which were taken with either the Prime Focus Universal Extragalactic Instrument (a.k.a. PFUEI) or the Double Spectrograph on the Hale 5-meter telescope. The following six clusters were discovered on the IV-N plates taken with the Mayall 4-meter telescope. Cluster CL0023+0423 has an unpublished redshift of 0.832. Cluster CL0231+0048 has an unpublished redshift of 0.60 or 0.69 and was known to have almost exclusively blue galaxies. Cluster 0943+4804 has an unpublished redshift of 0.698. Clusters CL1324+3011, CL1604+4304, and CL1604+4321 have published redshifts of 0.751, 0.895, and 0.918, respectively. Cluster CL2157+0347 was discovered on red image tube images taken with the Hale 5-meter telescope and has a published redshift of 0.820 (Gunn, Hoessel & Oke 1986). Images of some of these clusters can be found in Gunn, Hoessel & Oke (1986).

Two clusters, CL1325+3009 and CL1607+4109, were chosen from the Palomar Distant Cluster Survey (PDSCS), a CCD drift-scan survey taken with the Palomar 5-meter telescope and using the F555W and F785LP filters (Postman *et al.* 1996). The candidate clusters detected in this survey had only estimated redshifts which were based on the cluster profile and luminosity function of the galaxies. These two candidates are both from the supplemental PDSCS catalog which means they are of lower significance but their redshift estimates were close to unity making them desirable for spectroscopic follow-up. The estimated redshifts of CL1325+3009 and CL1607+4109 are 0.9 and 0.8, respectively.

The final list of clusters is given in Table 1 where the J2000 coordinates are used to identify the clusters (see above). Column 2 lists alternate IDs of the clusters as used by Gunn, Hoessel & Oke (1986) and Postman *et al.* (1996). The J2000 coordinates used for the cluster observations are given in columns 3 and 4, while the redshifts of the clusters and other groups in the line-of sight are listed in column 5 (for the spectroscopic reductions, see Sect. 4.2).

3. The Observations

3.1. Keck Broad-Band Observations

All of the optical observations, both broad band and spectroscopic, were carried out with the Low Resolution Imaging Spectrometer (LRIS; Oke *et al.* 1996) on either the Keck I or Keck II telescopes. In imaging mode LRIS has a field of 6×8 arcminutes. With the Tektronix 2048 \times 2048 back-illuminated and coated CCD with 24 \times 24 micron pixels, the sampling at the CCD is 4.65 pixels per arcsecond. Many of the observations were begun almost immediately after Keck I and LRIS were commissioned. Consequently the image quality was not at the optimum level. Even so, the full width half maximum for the images was

typically 0.8 to 1.0 arcsecond.

LRIS has a standard set of BVRI glass filters which match the Cousins system well. These filters must go in front of the camera lens and, consequently, are large. The B filter, however, is somewhat undersized because it was impossible to obtain a sufficiently large piece of Schott BG37 glass. As a result there is some vignetting in the B images which must be removed by the flat fielding. The mean wavelengths for the four LRIS filters are given in Table 2. Figure 1 shows the total system throughput (optics+detector+filter) for the LRIS BVRI passbands.

Previous observations at intermediate and high redshift (e.g. Butcher & Oemler 1984; Rakos & Schombert 1995) indicate that, at redshifts approaching unity, the cluster populations may be dominated by blue galaxies. Consequently, it was desirable to include observations in the B filter. Even though the night sky background is low in B, the total exposure time still had to be long since the quantum efficiency of the CCD is dropping towards the blue, and faint blue galaxies are still relatively red objects. At V the quantum efficiency is fairly high, and the night sky is still low while at R and I the quantum efficiency is near its peak, but the night sky is becoming bright.

The total exposure times in each filter are listed in Table 2 and were chosen to give fairly uniform errors in the photometry. The B, V, and R observations consisted of two equal exposures to allow for accurate cosmic ray rejection. The I exposure time was broken into 3 equal exposures in order to cope with the cosmic rays, as well as to avoid approaching too near to the CCD saturation level. In retrospect it would have been desirable to obtain about twice the total exposure in I. Typical AB magnitudes and fractional standard deviations ($AB \pm \sigma_{AB}$) of a representative galaxy at $z = 0.9$ in each filter are given in columns 4 through 6 of Table 2. Column 4 gives these values (as defined below) for a galaxy epoch of 0.7 Gyr, while the next two columns give similar data for galaxies whose epochs are 1.4 Gyr and 4.0 Gyr, respectively. These times are for Bruzual and Charlot (1993) models with a star formation rate that decreases with a time constant of 0.6 Gyr after time zero. Since errors are dominated by the sky brightness, the error in each band increases by approximately a factor of 2.512 when the value of AB increases by 1 magnitude.

The overall program was to obtain both broad-band images for photometry and slit-mask spectra. Therefore, if a night was photometric, the highest priority was given to broad-band photometry. If the sky was not photometric, spectra were obtained. An effort was made to obtain observations in all bands on the same night. All observations were made with LRIS rotated to a position angle on the sky of 180 degrees. In addition to the exposures, two kinds of flat fields were obtained. During each twilight, dome flats were taken with the telescope pointed to the zenith. Two nearly standard overhead projectors mounted on opposite sides of the primary mirror on the large telescope azimuth ring illuminated a round area on the surface of the dome directly in front of the primary mirror. The projectors have light shields so that only light which goes through the focusing lens enters the dome. The dome itself has a rippled surface on scales of about 100 mm and less and is painted with aluminum paint. The result is a fairly uniformly illuminated circle as seen by the telescope. The light level is suitable for exposures through the four BVRI filters. Flat fields were also obtained by looking at the twilight sky. One worry with such flat fields is that the light is highly polarized and therefore not really representative of the background night sky seen during the regular exposures. Since the flat fielding images were usually not adequate, another approach described below had to be invoked.

In order to calibrate the observations used to derive BVRI magnitudes on the standard Cousins-Bessell-Landolt (Cape) system, exposures were made of Landolt standard star fields (Landolt 1992). The

fields selected had between 3 and 8 stars spanning a wide range of colors all located within a single LRIS field of view. LRIS requires a minimum exposure time of 2 seconds to maintain uniformity over the field of view and it was, therefore, necessary to have the telescope out of focus by 2 mm for the Landolt fields. The fields observed are PG0231+051, Rubin 149, PG0918+029, PG1323-086, SA 107, Mark A, and SA 113. One, and occasionally two, of these fields were observed on each night that photometric observations were made.

3.2. Slit-Mask Spectroscopic Observations

Observations through slit-masks are the standard mode for observing many faint objects with LRIS. There is also a long slit option which is operationally identical to the slit-mask mode and is most useful for observing individual calibration stars. All of our spectral observations were made using the 300 g/mm grating which is blazed at 5000 Å. This grating provides a dispersion of 2.38 Å per pixel, and a spectral coverage of 5100 Å. The grating angle was set so that it provided coverage from approximately 4400 Å to 9500 Å in the first order. This range was chosen because it was anticipated that galaxies would be found with redshifts of at least 1.1, and it was imperative that the O[II] λ 3727 emission line always be in an accessible part of the spectrum. A GG495 glass filter was used to eliminate the overlapping second order spectrum; there is therefore no second order contamination below 9700 Å. Because slits are located at various positions in the focal plane, the wavelength range covered with any slit will deviate from the nominal range by up to approximately 600 Å in either direction.

The computer program to design slit-masks (Cohen 1995) can have as an input either accurate relative values of RA and Dec or positions measured in pixels from an image taken with LRIS. The latter input was used in almost every case. Additional parameters which are necessary are (a) position angle on the sky of the slit (always 180 degrees), (b) the appropriate hour angle anticipated, (c) the individual minimum slit length (8 arcseconds used to provide enough slit for sky subtraction), and (d) the slit width. Initially only two possible slit widths were available, 0.7 and 1.4 arcseconds. Because of the limited experience initially available with LRIS, it was decided to use the 1.4 arcsecond slit to minimize any problem in setting objects in the slits. A more ideal 1.0 arcsecond slit is now available and is being used for this program. The optical resolution of the spectrograph is a little less than 2 pixels. The 1.0 and 1.4 arcsecond slits, however, correspond to 4.6 and 6.5 pixels, respectively, so that the spectra are oversampled. All spectra were therefore smoothed with a running (1 2 3 4 3 2 1) weighting function.

One of the very early tasks was to obtain images of the clusters for the purpose of designing the slit-masks. The R filter was used for these preliminary cluster images because of the high CCD throughput in that passband and to optimize detection of distant cluster galaxies. Exposures of 600 sec in duration were taken under photometric or near photometric sky conditions. These were flattened using the dome flats already described and run through FOCAS (Valdes 1982) programs to generate object magnitudes and positions. Care was taken to fix any positions of close pairs not correctly deblended. An approximate extinction correction was applied, and the magnitudes corrected to proper R magnitudes. The range in right ascension was restricted to 600 pixels centered on the cluster. The range in declination was the full picture height of about 2000 pixels. A list of all objects brighter than approximately $R = 23.5 \pm 0.1$ in this box was then extracted in order to provide the list of candidates for slit-mask spectra. The uncertainty in the magnitude limit is dominated by flat-field residuals in these early data. The subsequent images obtained for our photometric analyses flattened to 1% or better. Typically, 200 galaxies satisfied the above criteria. Each mask can have about 35 slits and, thus, 6 masks were needed for each cluster. However,

the non-uniform galaxy distribution and the desire to observe some of the fainter targets more than once (for enhanced signal-to-noise and redshift consistency checks) impose a reduction in the number of targets observed down to approximately 130 – 150 objects per cluster field. In early slit-mask setups, for example CL0023+0423 and CL1604+4304, about 30 percent of the objects were observed more than once. In later setups about 10 percent of the objects were observed more than once. Two slit locations were always reserved for setup stars.

The high throughput of LRIS and the excellent image quality meant that we were able to achieve a signal-to-noise level sufficient to measure redshifts and study spectral features in a single 3600 sec exposure for each slit-mask. In the event of significant cloud coverage, two such exposures per mask were obtained.

To minimize the effects of instrument flexure, a combined Neon and Argon discharge lamp exposure was taken immediately following the object exposure. In addition, a flat field exposure was made using two quartz halogen lamp sources. Both the discharge and quartz halogen lamp radiation is reflected and scattered off the diffuse white underside of the dust cover which, when closed, is about 300 mm in front of the spectrograph slit-mask. The flat fields obtained in this way are excellent for flattening spectra and minimize any problems caused by flexure.

Since spectra were obtained at small zenith distances and the slits are fairly broad, it makes sense to try to calibrate the spectra approximately to relative absolute spectral energy distributions. This will at least remove the instrumental sensitivity. Spectra were, therefore, taken of standard stars using the same instrumental setup except that a long slit with a width of 1.4 arcseconds was used instead of a slit-mask. The standard stars were chosen from the list of faint HST standards by Oke (1992). Such spectra were taken at least once each night. They were always accompanied by discharge lamp and quartz halogen lamp exposures.

3.3. Infrared Observations at KPNO

For our high-redshift cluster sample, infrared imagery extends our ability to study the rest-frame optical spectral region which is dominated by the long-lived, near-solar mass stars, whereas the optical bands sample the poorly observed rest-frame ultraviolet, which is dominated by the short-lived, massive stars. Specifically, infrared imagery is well suited to examining the red, “passive” early-type population in high-redshift clusters (Gunn 1990; Aragón-Salamanca *et al.* 1993; Rakos & Schombert 1995; Stanford, Eisenhardt & Dickinson 1994; Lubin 1996). In addition, K-corrections in the infrared are smooth, better defined, and almost independent of Hubble type.

Therefore, we are in the process of carrying out deep infrared imaging of the cluster sample with the Infrared Imaging Camera (IRIM) on the Mayall 4m telescope at Kitt Peak National Observatory. IRIM contains a 256×256 NICMOS3 HgCdTe array which has a resolution of 0.60 arcsecond per pixel on the 4m telescope. The field-of-view (154×154 arcseconds) covers the central region of each cluster and corresponds almost exactly to the field-of-view of our Hubble Space Telescope (HST) imaging (see Sect. 3.4). We have chosen to make the deepest possible observations over this region and, thus, we have not mosaiced the entire LRIS field of view.

We observe in the $2.2\mu K'$ band. This intermediate band filter avoids the excessive thermal background in the wider K passband. Each central field is observed using a 4×4 dither pattern with a stepsize of $10''$ and a total extent of $30''$. Each exposure has an effective exposure time of 1 minute, with 4 co-additions of

individual, background-limited 15 second integrations. The total integration time on an individual cluster varies between 3 and 4.4 hours. Because the fields are not excessively crowded, we are able to use in-field dithering to create a global sky flat. Several HST standard stars from the list of Persson *et al.* (1997) are observed each night in five separate array positions for each star. Currently, observations have been made over 3 days in October 1996 and 2.5 days in March 1997.

3.4. HST WFPC2 Observations

Each of the nine cluster candidates in our sample has been or will be observed with the Wide Field Planetary Camera 2 (WFPC2) on the HST. The HST imaging covers one WFPC2 field of view (roughly $2' \times 2'$) of the central region of each cluster. The specifications of these observations, including the filters, exposure times, and current status, are given in Table 3. Two of the clusters, CL1324+3011 and CL1604+4321, were originally observed by J. Westphal in Cycle 4 (GO-5234) and have been obtained from the HST archive. The observations of the remaining seven clusters are being conducted in cycles 5 and 6 of the HST Guest Observer program (GO-6000, 6581; PI Postman).

The HST observations are being used to provide a detailed description of the structural characteristics of the galaxies detected in the central region of each cluster. The HST images for this survey are processed through the Medium Deep Survey (MDS; Griffiths *et al.* 1994) data reduction pipeline in order to objectively detect extended sources and provide a quantitative analysis of their structural properties. The brightest subsample of these galaxies are visually classified according to the Revised Hubble system of nearby galaxies given in e.g. the Hubble Atlas (Sandage 1961) and the Carnegie Atlas of Galaxies (Sandage & Bedke 1994). This subset corresponds to approximately 200 galaxies per field (corresponding to a limiting magnitude of $F702W \approx 24.7$). Two clusters, CL0023+0423 and CL1604+4304, currently have a completed set of spectroscopy, optical photometry, and WFPC2 observations. The results of the morphological studies for these clusters are presented in the third paper of this series (Lubin *et al.* 1997, hereafter Paper III). In this paper, we present a description of the calibration and reduction of the WFPC2 images, the object detection procedure, and the automated and visual galaxy classification (see Sect. 4.4).

4. Data Reduction

4.1. Keck Broadband Image Reduction

The LRIS imaging data were reduced in a fairly standard fashion. All frames were bias-subtracted and pixel-to-pixel sensitivity variations were removed using dome flats. Large-scale gradients were removed by dividing each frame by a normalized two-dimensional spline fit to the sky values in a sky-flat. The sky-flat was created by generating a median image from a stack of frames for each night and passband. For the I-band data, a two-dimensional fringe map was also created from the median filtered image by removing large-scale gradients within the median image. Fringing was then removed from each I-band frame by subtracting a suitably scaled version of the fringe map.

Excellent flat-fielding was achievable with the B and V band data with typical sky variations at the 0.2% level or less on scales of 20 arcseconds and larger. The R and I band images obtained prior to 1996 had some residual structure in the sky which may have been caused by unwanted illumination because the Cassegrain sky shield for Keck I had not yet been installed. However, the amplitude of these features was

typically at the 1.0% level (or less) on scales of 20 to 50 arcseconds. The left and right edges of all images were unusable due to vignetting from optics internal to LRIS. All image photometry was thus confined to the central 1500×2000 pixel region.

Image registration for a given cluster field was performed by identifying approximately 10 unsaturated stars (detectable in all 4 passbands) to be used as astrometric reference points. The mean X and Y offsets of these stars in every frame taken of the cluster were computed relative to their locations in a fiducial B-band image. All image data for the cluster were then shifted to match the B band coordinate system using a flux conserving Lagrangian interpolation scheme to achieve registration at the sub-pixel level. Once all frames of a given cluster were registered to a common coordinate system, the independent exposures in each passband were co-added to produce the final four BVRI images.

Absolute astrometry was performed by identifying objects on the LRIS CCD images that are also detected in digitized versions of the new Palomar Observatory Sky Survey. The number of such objects which are both unsaturated on the CCD and bright enough to yield accurate centroids on the digitized sky survey is small - usually no more than 12 objects. We then use the plate solution from the POSS-II data to astrometrically calibrate the CCD exposures. The typical rms error in our equatorial coordinates is about 0.8 arcsecond.

4.1.1. Object Photometry and Classification

We use the FOCAS package to detect, classify, and obtain aperture and isophotal magnitudes for objects in the co-added BVRI images. We generate independent object catalogs from the BVR images. However, we use the R-band isophotes to determine object parameters in the I-band images because the sky brightness increases significantly redwards of 7500 Å and object detection would have been severely compromised if done directly on the I-band image. Our isophotal detection threshold is set to be $3\sigma_{\text{sky}}$ which corresponds, on average, to $\mu_B = 27.4$, $\mu_V = 26.7$, and $\mu_R = 25.9 \text{ mag arcsec}^{-2}$, respectively. A minimum object area constraint of 0.55 arcsec 2 is also imposed for detection. Aperture magnitudes are computed using a circular aperture with a radius of 3 arcseconds (14 pixels). The limiting magnitudes are B = 25.1, V = 24.1, R = 23.5, and I = 21.7 for a 5- σ detection in our standard 3 arcsecond radius aperture. An aperture radius of 3 arcseconds corresponds to 12.8 and $14.9h^{-1}$ kpc at $z = 0.6$ and $z = 0.9$, respectively. This aperture choice is consistent with that used for faint galaxy photometry in other intermediate redshift cluster analyses (*e.g.*, Aragón-Salamanca *et al.* 1993, Smail, Ellis & Fitchett 1995, Barger *et al.* 1996).

To get optimal star/galaxy classification accuracy, the PSF is generated from a manually selected sample of unsaturated stars. We have found that on very deep frames, the automatic PSF star selection used in FOCAS can occasionally generate overly broad PSFs – the probable result of compact galaxies being included in the computations. Manual selection avoids this problem. The typical FWHM seeing in our LRIS image data is 0.96 arcsecond. About 25% of the data had FWHM seeing of 0.8 arcsecond.

Lastly, the objects in the BVRI catalogs are matched with one another using the *match* algorithm in FOCAS. This produces a catalog from which colors can be generated.

4.1.2. Conversion of BVRI to Absolute Flux AB

With 4 magnitudes in B, V, R, and I, the easiest and most instructive way to make comparisons with evolutionary models (e.g. Bruzual & Charlot 1993) is to convert them to absolute fluxes (AB) where AB is defined as

$$AB = -2.5 \log f_\nu - 48.60 \quad (1)$$

and f_ν is the flux in $\text{erg cm}^{-2} \text{ s}^{-1} \text{ Hz}^{-1}$. One can define ABB, ABV, ABR, and ABI for each band.

The conversion from BVRI to AB would be easy if one knew the transmission functions of the four bands, the CCD quantum efficiency, and the throughput of the telescope and spectrograph. Then, with a series of absolute spectral energy distributions for standard BVRI standard stars of different colors, one could perform integrations over each band and derive the conversions from BVRI to AB directly. One could also generate AB values for the evolutionary models which have constructed absolute energy distributions. Absolute energy distributions do exist for a number of BVRI standard stars; however, no adequate information about the details of the BVRI system exist, so one cannot easily convert the model magnitudes to the corresponding AB or BVRI magnitudes.

Therefore, a slightly different technique was used. The known filter, atmosphere, telescope transmission, and quantum efficiency functions for LRIS were used to generate a “natural” system which is close to but not identical with the BVRI system. The energy distributions for the standard BVRI stars were then used with these functions in order to generate natural magnitudes called “bvri.” Nearly all the standard BVRI stars used were taken from the list of faint spectrophotometric standard stars whose energy distributions had been measured for use with the Hubble Space Telescope (Oke 1992). BVRI magnitudes were kindly supplied by Landolt (1996). The natural bvri could also be easily generated for any of the evolutionary models being used. One could then derive relationships between bvri, BVRI and the ABs. The mean wavelengths for the ABs are those listed in Table 2. The derived conversions are as follows:

$$ABV = V + 0.01 \quad (2)$$

$$ABB = B - 0.091(B - V) - 0.09 \quad (3)$$

$$ABR = R + 0.034(V - R) + 0.17 \quad (4)$$

$$ABI = I - 0.121(V - I) + 0.44 \quad (5)$$

The color terms allow for the fact that the LRIS filters are not exactly at the standard BVRI wavelengths. The same transformations were used to convert absolute spectral energy distributions generated by evolutionary models to BVRI and ABs.

4.2. LRIS Spectrophotometric Reductions

The slit-mask images produced by LRIS consist of about 35 spectra, stacked vertically. Each spectrum spans the full width of the CCD. The raw spectroscopic images were bias-subtracted, flat-fielded, edited to remove cosmic ray hits, and rectified in both the spatial and dispersion directions. The uncalibrated spectra were then extracted after subtracting the sky as measured on both sides of each object spectrum. Comparison discharge-lamp spectra were extracted using the identical procedure and the emission line

positions fitted with a third order polynomial. The least-squares fit is accurate to about $0.2 - 0.5 \text{ \AA}$ at any point. The standard star spectra were processed identically. All object spectra were corrected for atmospheric extinction with the O_2 and water vapor absorption handled with a separate extinction law. The unknown spectra were converted as well as possible into absolute fluxes AB by dividing the unknown by the standard star observed flux.

The final spectra are approximately relative absolute energy distributions. They are approximate and relative because the spectra are not slitless and individual objects may not be centered precisely on the slits. Spectra are also sometimes taken in non-photometric conditions.

The majority of objects were faint and photon shot-noise was nearly always dominant. Sky subtraction of the $\lambda 5577$ or $\lambda\lambda 6300, 6363$ feature was always relatively poor because the lines are extremely strong. In the near infrared there are many OH^+ emission bands which are strong, and sky subtraction is relatively poor. A further serious problem above 8000 \AA is the fringing in the CCD which proved difficult to eliminate completely. The OH^+ emission bands, the fringing, and the rapidly decreasing quantum efficiency of the CCD mean that above 8000 \AA the spectra rapidly deteriorate in quality. Only very strong emission lines can be identified unambiguously.

4.2.1. Redshift Determination

Since most of the objects observed are fainter than $R=21$, their spectra can be quite noisy; in some cases the continuum has a signal-to-noise ratio approaching unity as R approaches 23.3. Emission lines, when present, have a higher S/N and are relatively easy to detect. Thus, a redshift measurement procedure which relies, in part, on visual inspection was used. The sky-subtracted two-dimensional spectrum was first displayed, and the pixel locations of all strongly suspected emission and absorption lines were recorded. The criterion for a line to be noted was that it have the proper shape along the dispersion and also stretch from one side of the spectrum to the other. Apparent emission or absorption features near the positions of strong sky emission lines were left out unless they were at least partially resolved from the night sky line. One could then look at the pattern of emission and absorption lines and infer the identifications. The emission lines usually seen were $[\text{OII}]\lambda 3727$, $\text{H}\beta$, $[\text{OIII}]\lambda\lambda 4959, 5007$, and $\text{H}\alpha$, or a subset of these depending on the redshift. Absorption lines are much harder to see visually and only H and K were normally seen. Once emission lines and/or H and K were identified one could often identify the other strong absorption features $\lambda 3835$ blend, $\text{H}\delta$, $\text{H}\gamma$, the G-band, and $\text{H}\gamma$ in the plotted spectrum. The spectrum was then plotted on a very expanded scale around each suspected line and the center of each well defined feature determined. This could easily be done to a precision of 1 \AA (typical instrumental resolution is $\sim 11 \text{ \AA}$). A redshift was calculated for each line, and an average taken of all the detected lines. In a few objects other emission lines such as the $[\text{NeV}]\lambda\lambda 3869, 3968$, $[\text{NII}]\lambda\lambda 6548, 6583$, and $[\text{SII}]\lambda\lambda 6716, 6730$ were seen.

At redshifts near unity one often runs into the problem that only one emission line is seen. The line could be $\text{H}\alpha$, $[\text{OIII}]\lambda 5007$, $\text{H}\beta$, or $[\text{OII}]$. In some cases an identification with $\text{H}\alpha$ can be ruled out because the $\text{H}\beta$ / $[\text{OIII}]$ group is not seen in the part of the spectrum where it could easily be detected. Similarly, one can rule out $\text{H}\beta$ / $[\text{OIII}]$ because $[\text{OII}]$ is missing. It was sometimes possible to confirm the identification with $[\text{OII}]$ by the presence of the absorption features $\text{MgII}\lambda\lambda 2795$ and 2802 (occasionally resolved) and $\text{FeII}\lambda\lambda 2586, 2600$.

There are a few spectra where no spectral features are seen even though the signal-to-noise level is relatively high. These are probably cases where $z < 0.2$ or $z > 1.5$ and, thus, the portion of the spectrum

sampled has only very faint features. In a few cases where $z < 0.2$ there is evidence for the Na D lines in absorption. There are also spectra with very low signal-to-noise levels. In these cases one can only assume that very strong emission lines are not present. The sample of spectra always contained a few faint stars. Their zero redshifts were usually verified by the presence of the D lines and $\text{H}\alpha$. Some of the stars were M stars with TiO bands which were easily identified even in noisy spectra. Figure 2 shows our final redshift measurement efficiency as a function of R magnitude. The probability of measuring a redshift, either galaxy, quasar, or star, is about 90% of the objects observed.

If an object is observed more than once, then its redshift is quite accurate. In the few cases where multiple observations of the same galaxy yielded different redshifts, we were always able to resolve the discrepancy. In some cases two emission lines would be seen in one spectrum and only one in a second poorer spectrum. In the spectrum with only one line the line was misidentified. Occasionally, an object was misidentified. For the objects with only a single observation (70 to 90% depending on the specific cluster), there is about a 10% chance that a gross error has been made in the z . The typical instrumental error is 0.0006 in redshift which corresponds to 180 km sec $^{-1}$ at $z = 0.0$ and 95 km sec $^{-1}$ at $z = 0.90$.

Figure 3 shows the redshift histograms for the nine clusters in the survey. The redshifts presented here are geocentric values. Six of the nine candidate clusters of galaxies are real space density enhancements. They are CL0023+0423, CL0943+4804, CL1324+3011, CL1325+3009, CL1604+4304, and CL1604+4321. The velocity dispersions of these 6 systems range from 400 km sec $^{-1}$ to 1300 km sec $^{-1}$ and are typical of clusters at low and intermediate redshifts. CL1604+4304 and CL1604+4321 have similar redshift distributions suggesting the existence of a supercluster system. A more detailed analysis of the photometric and spectral data of the first two clusters with complete data, CL0023+0423 and CL1604+4304, are presented in the second paper of the series (Postman, Lubin & Oke 1998, hereafter Paper II).

4.3. IRIM Reduction and Object Detection

The K' cluster data are reduced using the Deep Infrared Mosaicing Software (DIMSUM), a publicly available package of IRAF scripts. The data are linearized, trimmed to exclude masked columns and rows on the edges of the arrays, and dark-subtracted using dark frames of the same exposure length as the observations. Testing by the authors and others (M. Dickinson and A. Stanford) have shown that the best flat-fielding in K' is obtained with dome flats taken with the lights off. All images of a given night are flattened by a super flat made from a series of dome flats taken during the previous day. As part of the DIMSUM procedure, sky subtraction is done by subtracting a scaled median of nine temporally adjacent exposures for each frame. We have chosen nine exposures for this procedure as it provides a good statistical sample of the sky values over a time period where we typically expect the sky variations to be stable. A first-pass reduction is used to create an object mask for each frame. This mask is created from a fully stacked mosaic image. It, therefore, excludes not only the bright objects, but also those objects too faint to be detected in an individual exposure. In the second pass, the object mask is used to avoid object contamination of the sky flat in the production of sky frames. Final mosaicing of the images of each cluster are made with a replication of each pixel by a factor of 4 in both dimensions. This procedure conserves flux while eliminating the need for interpolation when the individual frames are co-aligned. That is, there is sufficient resolution that only integer shifts are necessary when co-adding the individual frames. A bad pixel mask is used to exclude bad pixels from the final summed images. Object detection is carried out on the final sum of the K' images.

Object detection, cataloging, and photometry are done using the the SExtractor image analysis package (Bertin & Arnouts 1996). The isophotal detection threshold is set at the $1.5\sigma_{\text{sky}}$ level which corresponds to, on average, $\mu_{K'} = 22.2 \text{ mag arcsec}^{-2}$. A 7×7 pixel top-hat spatial filter and a minimum detection area of 35 pixels are also used. Here, “pixel” refers to the “subpixels” of the original image, i.e. the $0''.15$ pixels that result after the 4×4 replication described above. A typical FWHM of a star in the summed image is 1.0 arcsecond. One of us, MP, has explored potential systematic differences between FOCAS (used for the optical image analysis) and SExtractor. No significant differences in photometry, astrometry, or classification were found providing the object detection parameters are set identically.

Absolute photometric transformations are derived from the observations of Persson *et al.* (1997) standard stars. Each standard is observed five times; first in the center of the array, and then near each of the four corners. These images are dark-subtracted and flat-fielded in the same manner described above for the cluster images. The five standard star images are then combined into a “local sky” frame using the median percentile clipping option in the IRAF task IMCOMBINE. The resulting sky image is subtracted from each of the five standard star images. The instrumental magnitudes of the star are then measured. The mean instrumental magnitude of the five individual measurements is used as the assigned instrumental magnitude of that standard star. The typical standard deviation of these mean instrumental magnitudes is 0.03 mag or less. The typical variations about the nightly photometric transformations are 0.02 mag or less. Although a fraction of the observations were carried out in non-photometric conditions, enough photometric data were obtained for each cluster to ensure absolute calibration to the required precision of < 0.03 mag. The conversion from this Vega-based to the AB magnitude system (see Sect. 4.1.2) is given by

$$ABK' = K' + 1.86 \quad (6)$$

For this project, we would like to reach a limiting magnitude of $K' = 20$ for a 5σ detection in our standard aperture of radius $3''.0$. The limiting magnitudes of our optical observations (see Sect. 4.1.1) indicate that this limit is appropriate for the bluest cluster members at these redshifts. Currently, three out of the nine clusters have been completed down to this limiting magnitude. Future observations to complete the survey are planned. The first results from the infrared survey will be presented in Lubin, Oke & Postman 1998.

4.4. WFPC2 Data Reduction

The Medium Deep Survey (MDS) team has devoted considerable effort to improving the calibration procedure of WFPC2 images. Such improvements are essential to the quantitative analysis of the faintest extended sources in these images. Since we would like to extend our analyses to low signal-to-noise ratios, we have used the final, calibrated images from the MDS reduction pipeline for both the automated and the visual galaxy classifications of our HST fields. We briefly describe their data reduction procedure below; however, the complete details can be found in Ratnatunga, Ostrander & Griffiths (1997; hereafter referred to as ROG), Ratnatunga *et al.* (1994, 1995), and at the MDS website address <http://astro.phys.cmu.edu/mle/index.html>.

The WFPC2 images are calibrated using the best available calibration data. Presently, these data come from the calibration files created by the Space Telescope Science Institute (STScI) to calibrate the Hubble Deep Field (HDF; Williams *et al.* 1996). Therefore, the static mask, super-bias, super-dark, and

flat field calibration files of the HDF are adopted for this procedure. Hot pixel tables from STScI for the given observation period are used to correct warm pixels. Hot pixels which cannot be corrected to an acceptable accuracy, saturated pixels, and pixels with a large dark current are ignored. The MDS software is designed to handle excluded pixels.

A corrected version of the standard IRAF/STSDAS combine task is used to create a stacked image (see ROG and Ratnatunga *et al.* 1994 for the specifics of this stacking procedure and the associated statistical errors). The individually calibrated images are stacked with shifts that correspond to the nearest integer number of pixels. Slight variations in the mean sky background are taken into account by allowing for a mode offset between pointings. This procedure produces the final reduced image used for the morphological studies. We have verified the MDS procedure by reducing the HST observations separately using the standard STSDAS routines. The relative positions and fluxes of over 100 galaxies per field were compared. No significant differences were observed; the scatter was consistent within the statistical uncertainties.

4.4.1. Object Detection in WFPC2 Images

After the images are stacked, the automated object detection is then performed using a “find” algorithm developed by the MDS team specifically for WFPC data. Because the algorithm does not perform any pre-convolution of the data, it is insensitive to hot or missing pixel values (see above). The detection algorithm is based on finding local maxima in the field. Nearby pixels are then mapped and associated with that particular maxima. Detections significantly above the noise are cataloged, and a “mask” image is made. A canonical radius of 0.5” is chosen as the object resolution, so that individual galaxies are not split into smaller components. All maxima within this radius are merged with the brightest center.

The resulting mask is examined for bright objects which have been over-resolved and for ghost images or bright stellar diffraction spikes which have been mistakenly detected as objects. These spurious detections are interactively flagged for rejection or merger with the central image. This interactive procedure follows a well-defined set of guidelines which have been adapted for WFPC2 data. For more details on this procedure, see the references given above.

4.4.2. Automated Object Classification in WFPC2 Images

The last part of the MDS pipeline is a two-dimensional maximum likelihood image analysis procedure which automatically optimizes a model and the number of parameters to be fit to each object image. Two scale-free, axisymmetric models are chosen to describe the galaxy profiles. Elliptical galaxies are assumed to have a bulge-like profile of $e^{-r^{1/4}}$, while disk galaxies have a disk-like profile of e^{-r} . Here, r is the radial distance from the galaxy center. Each profile is characterized by a major axis half-light radius and axis ratio. Stellar (point-like) objects are examined through the same procedure as the galaxy images, except a Gaussian e^{-r^2} profile is adopted.

For most of the galaxies, a 64-pixel square region around the center of galaxy is examined. For larger galaxies, a 128-pixel square region is chosen. The mask of detected objects (see above) is used to determine a contour around each object which is 1σ above the estimated local sky. The total integrated signal-to-noise ratio of these pixels is a good measure of the information content of the image. The completeness limit of the object finding algorithm is $SNRIL \sim 1.5$, where $SNRIL$ is the decimal logarithm of the integrated signal-to-noise ratio. However, only those galaxies with $SNRIL > 2$ have enough signal to be reliably fit

to the full two-component model discussed above (see ROG).

A full two-component model is fit to all objects with $SNRIL > 2$; however, extensive testing has shown that galaxies with $SNRIL < 2$ do not have sufficient signal to be fit to a model with such a large number of parameters. Therefore, these images are examined only as a pure disk, a pure bulge, or a stellar object. As a first pass, each object is fit to a disk-like model if $SNRIL \leq 2$ or a 10-parameter disk + bulge model if $SNRIL > 2$. If the half-light radius is less than one pixel, a stellar profile is also fitted. The star-galaxy classification is based on both the likelihood ratio for the best galaxy model and the half-light radius. In addition, the following checks are also made. Firstly, for those images originally fit by a two-component disk + bulge model, a single-component model with fewer parameters is examined to determine whether the two-component model is a significantly better fit. Secondly, for images with a half-light radius less than two pixels, a single-component fit is selected, as these galaxy images are too undersampled to give realistic two-component models.

A maximum likelihood parameter estimation procedure is used to determine the best model and parameter values. For each set of model parameters, a model image of the object is created and compared with the actual object image. The likelihood function is defined as the product of the probabilities for each model pixel value with respect to the observed pixel value and its error distribution. This function is minimized by a routine described in Ratnatunga & Casertano (1991). Finally, a best-fit model and its parameters are determined for each object with the following classifications : bulge + disk, disk, bulge, galaxy (if the classification as disk or bulge is not significant), stellar, or object (if there is no preference between star and galaxy). For the fine details on the parameter fittings and the maximum likelihood estimator, see ROG and the references listed above.

All of those objects classified as non-stellar down to the completeness limit of $SNRIL > 1.5$ are presented; however, only those galaxies with a reliable signal-to-noise ($SNRIL > 2$) are used in the morphological analyses in Paper III. The magnitude to which this signal-to-noise corresponds depends on the duration and passband of the particular observation (see Table 3), e.g. a $SNRIL = 1.5$ corresponds to $F702W \simeq 26.3$ and $F814W \simeq 26.0$ for a stellar object in the CL0023+0423 and CL1604+4304 fields, respectively. The catalogs and the first results from the automated galaxy classifications of these two cluster fields are presented in Paper III.

4.4.3. Visual Classification of Galaxies in WFPC2 Images

In addition to the automated classifications, we have also performed a visual classification of the brightest galaxies detected in the MDS automated object detection procedure described in Sect. 4.5.1. For each individual HST observation, we determine the total magnitude limit down to which we can accurately classify galaxies by eye. We define the total magnitude of each galaxy as the analytic total magnitude of the best-fit galaxy model determined in the automated classification procedure (see Sect. 4.5.2). The magnitude limit that we choose depends on the specifics of the individual cluster observation (e.g. $F702W = 24.7$ for CL0023+0423 and $F814W = 24.3$ for CL1604+4304; see Paper III). These limits correspond to ~ 200 galaxies per field.

We base our visual classifications on the Revised Hubble scheme, that is, the standard galaxy classification systems used in the Hubble Atlas (Sandage 1961) and the Carnegie Atlas of Galaxies (Sandage & Bedke 1994). The assignment of morphological types on the Revised Hubble Type system is made by a visual inspection of images displayed using IRAF and SAOIMAGE. A $60'' \times 60''$ pixel grey scale image

centered on each galaxy brighter than our chosen magnitude limit is examined. Each image is stretched at 0–100DN and 0–400DN, using a logarithmically scaled display. This display provides the wide dynamic range necessary to detect both low surface brightness features in the outer regions of the galaxy, as well as the high surface brightness structure in the galaxy core. Furthermore, it most closely mimics the response of photographic plates, which are the source of the historical galaxy classification scheme. In addition to our display techniques, we have used the CCD survey by Frei *et al.* (1996) of 113 nearby galaxies as a reference sample in order to compare directly our CCD images of high-redshift galaxies to those galaxies in the local universe. These observations were made in either B_j and R or g , r , and i . All of the Frei *et al.* galaxies have classifications based on photographic plates (see the Carnegie Atlas of Galaxies).

For the specifics of the galaxy classifications, we have adopted the classification procedure first employed by Dressler *et al.* (1994) for an HST study of galaxies in the field of the cluster CL0939+4713 at $z = 0.41$, and adopted by Smail *et al.* (1997) for a comprehensive catalog of morphological types in 10 intermediate redshift clusters. This galaxy classification includes four components : (1) Revised Hubble type, (2) disturbance index – the perceived asymmetry of the galaxy image, (3) dynamical state – the interpretation of the cause of any observed disturbance and (4) comments. The disturbance index (D) ranges from 0 to 4 with the following definitions : 0 – little or no asymmetry, 1 or 2 – moderate or strong asymmetry, and 3 or 4 – moderate or strong distortion. This classification was intended to be objective in that it is independent of the possible reason of the disturbance. The “dynamical state,” however, was intended to be a subjective and interpretive judgment of the cause of the disturbance and should, therefore, be viewed only as an educated guess. The classes assigned to this parameter are : I – tidal interaction with a neighbor, M – tidal interaction suggesting a merger, T – tidal feature without obvious cause, and C – chaotic. For more details on these four components, see Smail *et al.* (1997) and Paper III. All of the galaxies in our HST images are classified by L. Lubin and M. Postman; in addition, A. Sandage kindly provides expert classifications of the galaxy samples. In particular, he reviews the rather tricky separation between elliptical (E) and S0 galaxies. The independent classifications are merged by L. Lubin.

In Paper III, we present the results of our morphological study of the clusters CL0023+0423 and CL1604+4304. This paper includes full catalogs of the automated and visual galaxy classifications in these fields, a comparison between the two classification methods, and a study of the cluster galaxy populations.

5. Summary

We have described the data acquisition and reduction procedures of our photometric and spectroscopic campaign to study nine candidate clusters of galaxies at redshifts of $z > 0.6$. The observational program consists of four main parts :

1. Spectra for approximately 80% of all galaxies down to a Johnson–Cousins R magnitude of ~ 23.5 within a fixed area of $2'.2 \times 7'.6$ of each cluster field using the Low–Resolution Imaging Spectrograph (LRIS) at the Keck 10m telescope. We have obtained spectra covering the range 4400 Å to 9500 Å for ~ 130 –150 galaxies per cluster field. Redshifts have been determined for 892 objects.
2. Deep $BVRI$ imaging with Keck of all galaxies in the full LRIS field of $6' \times 8'$ centered on each cluster. The 5σ detection limits are $B = 25.1$, $V = 24.1$, $R = 23.5$, and $I = 21.7$ in our standard 3 arcsecond radius aperture. The photometric data are converted to absolute fluxes in order to obtain absolute spectral energy distributions.

3. High angular resolution imagery with HST in order to provide morphological information on the galaxies in the WFPC2 field-of-view ($160'' \times 160''$) centered on each cluster. Each of the cluster candidates has been or will be observed by HST in Cycles 5 and 6.
4. High precision K band photometry across the WFPC2 field-of-view with the KPNO 4m telescope for each cluster. The infrared survey reaches a limiting magnitude of $K' = 20$ in the standard aperture.

We have presented the redshift histograms for the nine candidate clusters of galaxies in this survey. We find that six of the nine candidate clusters of galaxies are real density enhancements. They include CL0023+0423, CL0943+4804, CL1324+3011, CL1325+3009, CL1604+4304, and CL1604+4321. The remaining three candidates are of a more dubious nature. Their redshift distributions reveal no clear density enhancement but rather an apparent superposition of small groups of galaxies along the line-of-sight. This false positive rate is consistent with the estimate of $\sim 30\%$ provided in Postman *et al.* (1996). At lower redshifts ($z \lesssim 0.5$) the spurious rate is about 20% or less. This is based on spectroscopic follow-up of PDCS candidates being done by Holden & Nichol (1998) at the KPNO 4m telescope. We conclude that optical detection of clusters remains a successful and important method for identifying such systems out to $z \sim 1$ and, further, will provide an important complement to cluster searches at other wavelengths.

Results on the star-formation history, dynamics, and morphological properties of CL0023+0423 ($z = 0.84$) and CL1604+4304 ($z = 0.90$) are presented in Papers II and III.

We thank Don Schneider and the anonymous referee for their invaluable comments on this manuscript. The W.M. Keck Observatory is operated as a scientific partnership between the California Institute of Technology, the University of California, and the National Aeronautics and Space Administration. It was made possible by the generous financial support of the W. M. Keck Foundation. LML graciously acknowledges support from a Carnegie Fellowship. Support for this work was also provided, in part, by NASA through grant number GO-06000.01-94A from the Space Telescope Science Institute, which is operated by the Association of Universities for Research in Astronomy, Inc., under NASA contract NAS5-26555.

REFERENCES

Abell, G.O. 1958, *ApJS*, 3, 211

Abell, G.O., Corwin, H.G. & Olowin, R.P. 1989, *ApJS*, 70, 1

Aragón-Salamanca, A., Ellis, R.S., Couch, W.J. & Carter, D. 1993, *MNRAS*, 262, 764

Barger, A. J., Aragón-Salamanca, A., Ellis, R. S., Couch, W. J., Smail, I., & Sharples, R. M. 1996, *MNRAS*, 279, 1

Bertin, E. & Arnouts, S. 1996, *A&A*, 117, 393

Bruzual, A.G. & Charlot, S. 1993, *ApJ*, 405, 538

Butcher, H. & Oemler, A. 1984, *ApJ*, 285, 426

Carlberg, R.G., Morris, S.L., Yee, H.K.C. & Ellingson, E. 1997, *ApJ*, 479, 19

Cohen, J. 1995, (private communication).

Dalton, G.B., Efstathiou, G., Maddox, S.J. & Sutherland, W.J. 1994, *MNRAS*, 269, 151

Dressler, A. 1980, *ApJS*, 42, 565

Dressler, A. & Gunn, J.E. 1992, *ApJS*, 78, 1

Dressler, A., Oemler, A., Butcher, H.R. & Gunn, J.E. 1994, *ApJ*, 430, 107

Dressler, A., Oemler, A., Couch, W.J., Smail, I., Ellis, R.E., Barger, A., Butcher, H., Poggianti, B.M. & Sharples, R.M. 1997, *ApJ*, 490, 577

Ellingson, E., Yee, H.K.C., Abraham, R.G., Morris, S.L., Carlberg, R.G. & Smecker-Hane, T.A. 1997, *ApJS*, 113, 1

Ellis, R.S., Smail, I., Dressler, A., Couch, W.J., Omeler, A., Butcher, H. & Sharples, R. 1997, *ApJ*, 483, 582

Griffiths, R.E. *et al.* 1994, *ApJ*, 435, L19

Gunn, J. E., Hoessel, J. G. & Oke, J. B. 1986, *ApJ*, 306, 30

Gunn, J.E. 1990, in *Clusters of Galaxies*, eds. W.R. Oegerle *et al.*, p. 341

Holden, B., & Nichol, R. C. 1998, private communication.

Landolt, A. U. 1992, *AJ*, 104, 340

Landolt, A. U. 1996, (private communication)

Lubin, L.M. 1996, *AJ*, 112, 23

Lubin, L.M., Oke, J.B. & Postman 1998, *AJ*, in preparation

Lubin, L.M., Postman, M., Oke, J.B., Ratnatunga, K.U., Gunn, J.E., Hoessel, J.G. & Schneider, D.P. 1998, *AJ*, submitted (Paper III)

Lumsden, S.L., Nichol, R.C., Collins, C.A. & Guzzo, L. 1992, MNRAS, 258, 1

Oke, J. B., Gunn, J. E. & Hoessel, J. G. 1996, AJ, 111, 29

Oke, J. B. 1990, AJ, 99, 1621

Oke, J. B., *et al.* 1995, PASP, 107, 375

Oke, J. B., Gunn, J.E. & Hoessel, J.G. 1996, AJ, 111, 29

Persson, S.E. *et al.* 1997, AJ, submitted

Postman, M., Lubin, L. M., Gunn, J. E., Oke, J. B., Hoessel, J. G., Schneider, D. P. & Christensen, J. 1996, AJ, 111, 615

Postman, M., Lubin, L. M. & Oke, J. B. 1998, AJ, submitted (Paper II)

Rakos, K.D. & Schombert, J.M. 1995, ApJ, 439, 47

Ratnatunga, K.U. & Casertano, S. 1991, AJ, 101, 107

Ratnatunga, K.U., Griffiths, R.E., Casertano, S., Neuschaefer, L.W. & Wyckoff, E.W. 1994, AJ, 108, 2362

Ratnatunga, K.U., Griffiths, R.E., Neuschaefer, L.W. & Ostrander, E.J. 1995, in Proc. HST Calibration Workshop II, eds. A. Koratkar and C. Leitherer, p. 351

Ratnatunga, K.U., Ostrander, E.J. & Griffiths, R.E. 1997, ApJ in preparation (ROG)

Sandage, A. 1961, The Hubble Atlas, The Carnegie Institution of Washington Publication

Sandage, A. & Bedke, J. 1994, The Carnegie Atlas of Galaxies, The Carnegie Institution of Washington Publication

Shectman, S. 1985, ApJS, 57, 77

Smail, I., Ellis, R. E., & Fitchett, M. J. 1995, MNRAS, 279, 245

Smail, I., Dressler, A., Couch, W.J., Ellis, R.E., Oemler, A., Butcher, H.R. & Sharples, R.M. 1997, ApJS, 110, 213

Stanford, S.A., Eisenhardt, P.R.M. & Dickinson, M. 1995, ApJ, 450, 512

Stanford, S.A., Eisenhardt, P.R.M. & Dickinson, M. 1995, ApJ, 492, 461

Valdes, F. 1982, Proc. SPIE, 331, 465

Williams, R.E. *et al.* 1996, AJ, 112, 1335

Yee, H.K.C., Ellingson, E. & Carlberg, R.G. 1996, ApJS, 102, 269

Zwicky, F., Herzog, E., Wild, P., Karpowicz, M. & Kowal, C.T. 1968, Catalogue of Galaxies and Clusters of Galaxies, California Institute of Technology, Pasadena

Table 1 : The Cluster Sample

Cluster	Alternate ID	R.A. (2000)	Dec. (2000)	Redshifts
CL0023+0423	00 21 18 +04 06 30	00 23 52.2	+04 23 07.4	0.63(6), 0.72(5), 0.84(25), 0.92(4), 1.10(4)
CL0231+0048	02 29 09 +00 35 30	02 31 43.2	+00 48 44.0	0.28(12), 0.58(9), 0.62(4), 0.75(5), 0.80(8), 1.00(9)
CL0943+4804	09 40 25 +48 19 00	09 43 41.0	+48 04 45.5	0.41(6), 0.47(13), 0.70(10), 0.94(4)
CL1324+3011	13 22 27 +30 27 18	13 24 50.4	+30 11 25.8	0.59(4), 0.66(4), 0.76(15)
CL1325+3009	PDCS S14	13 25 18.7	+30 09 57.0	0.40(11), 0.62(7), 0.67(7), 0.72(12), 0.92(7), 1.07(11), 1.20(3)
CL1604+4304	16 02 44 +43 12 54	16 04 19.5	+43 04 33.9	0.50(8), 0.83(7), 0.90(22)
CL1604+4321	16 02 44 +43 29 24	16 04 31.6	+43 21 35.4	0.24(6), 0.46(5), 0.62(6), 0.70(8), 0.93(39)
CL1607+4109	PDCS S23	16 07 30.9	+41 09 32.0	0.56(6), 0.60(6), 0.77(5), 0.92(3)
CL2157+0347	21 55 19 +03 34 12	21 57 52.2	+03 47 00.0	0.45(8), 0.64(5), 0.82(5), 0.85(4), 1.10(3)

Table 2 : The Broad Band Photometric System

Filter	Wavelength (Å)	Exposure Time (sec)	Galaxy at $z = 0.90$		
			Age = 0.7 Gyr	Age = 1.4 Gyr	Age = 3.0 Gyr (AB $\pm \sigma_{AB}$)
B	4416	3600	22.30 ± 0.02	23.00 ± 0.03	25.10 ± 0.23
V	5458	2000	22.14 ± 0.03	22.60 ± 0.05	23.57 ± 0.12
R	6384	1200	21.87 ± 0.04	22.12 ± 0.05	22.51 ± 0.07
I	8424	900	21.00 ± 0.08	21.00 ± 0.08	21.00 ± 0.08

Table 3 : The HST Observations

Cluster	Filter	Duration (ksec)	Cycle	Status
CL0023+0423	F702W	17.9	5	Observed Nov 1995 (GO-6000)
CL0231+0048	F606W	15.3	5	Observed Nov 1995 (GO-6000)
CL0943+4804	F702W	18.8	6	To be observed in 1998 (GO-6581)
CL1324+3011	F606W	16.0	4	Archival data (PI Westphal; GO-5234)
	F814W	32.0	4	Archival data (PI Westphal; GO-5234)
CL1325+3009	F814W	18.8	6	To be observed in 1999 (GO-6581)
CL1604+4304	F814W	64.0	4	Archival data (PI Westphal; GO-5234)
CL1604+4321	F702W	18.8	6	Observed Dec 1997 (GO-6581)
CL1607+4109	F702W	18.6	5	Observed Jul 1997 (GO-6000)
CL2157+0347	F702W	18.8	6	Observed Jul 1997 (GO-6581)

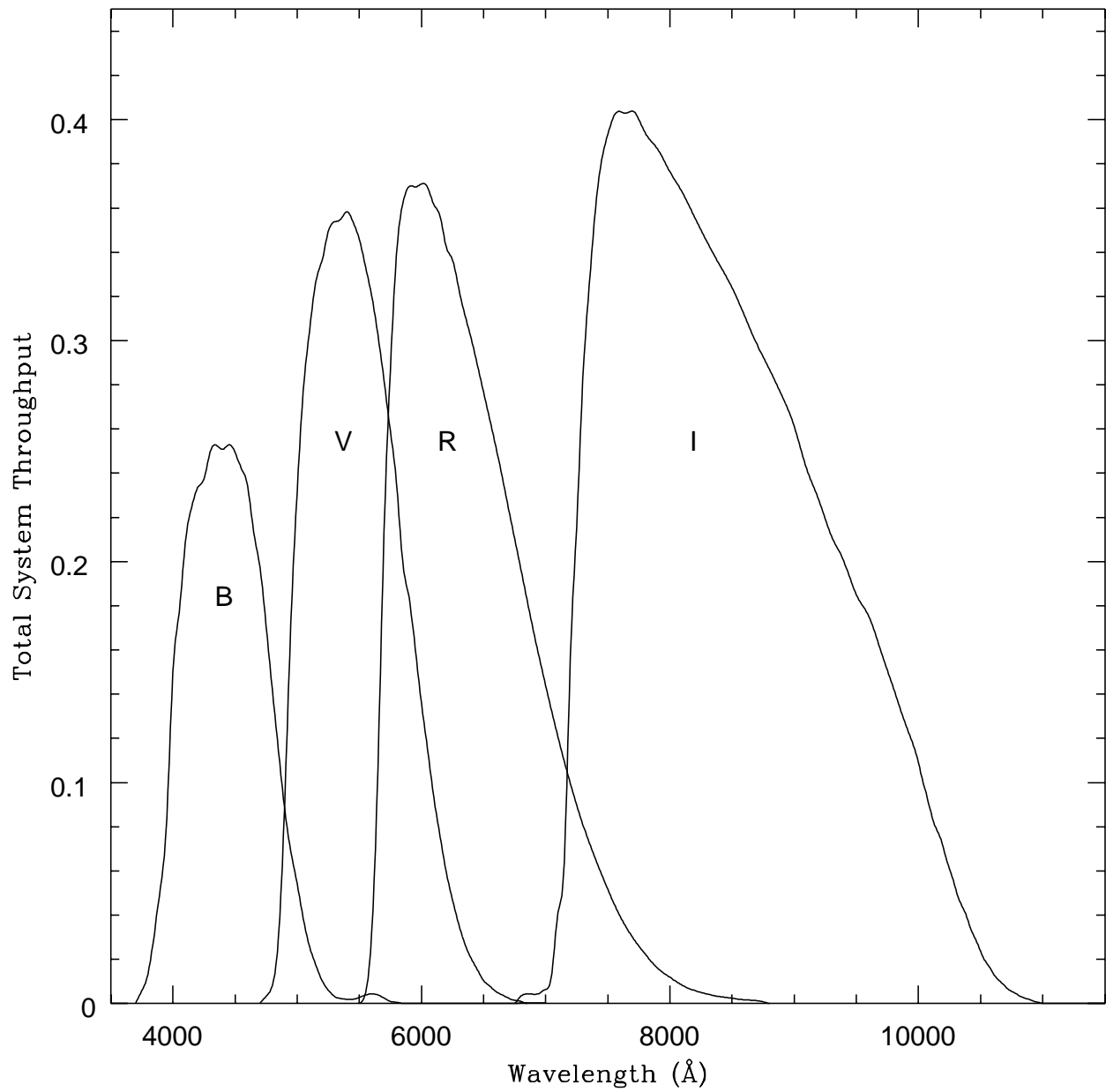


Fig. 1.— The response curves of the optical filter set.

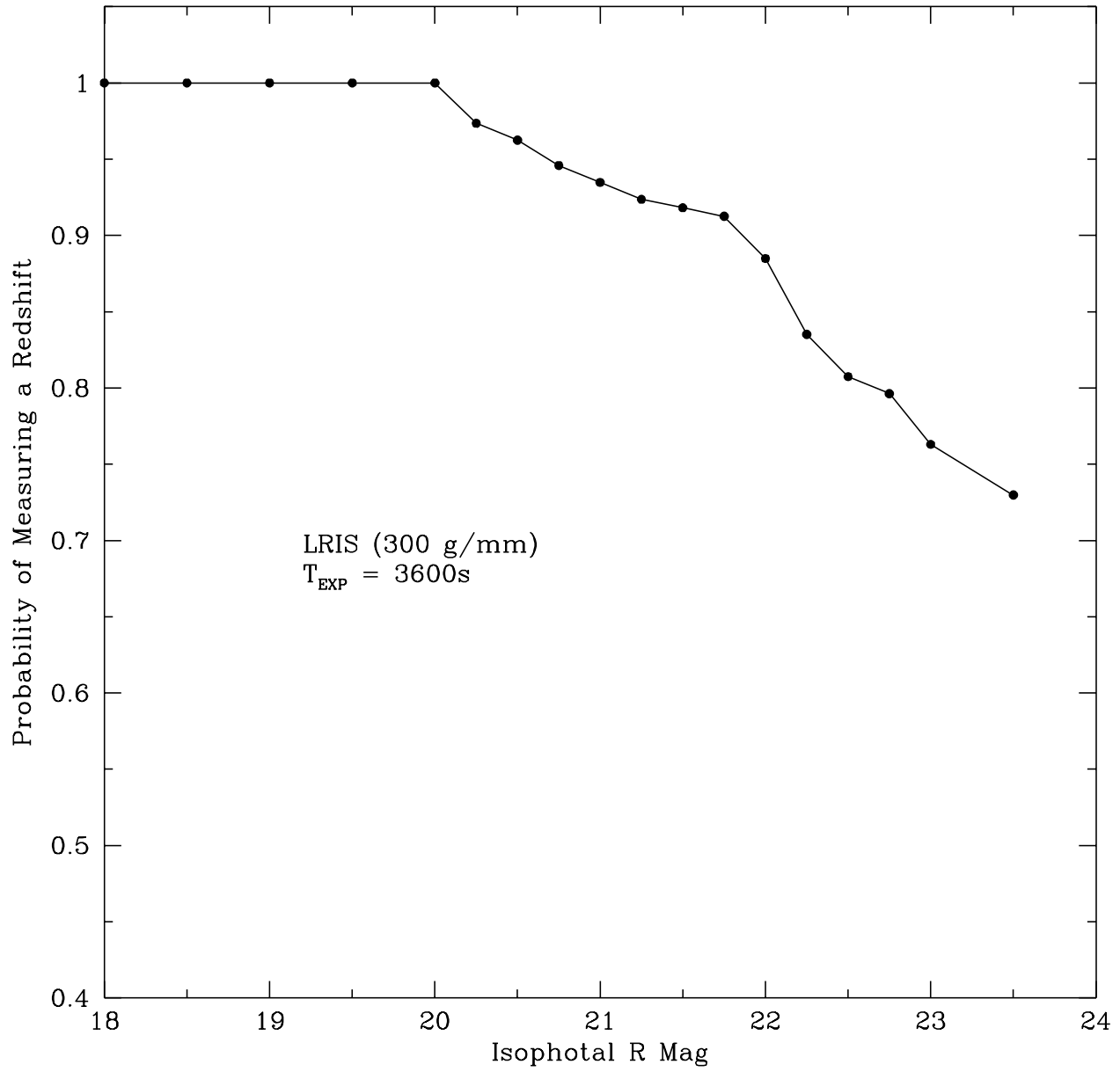


Fig. 2.— Fraction of spectra for which redshifts were successfully measured as a function of isophotal R magnitude.

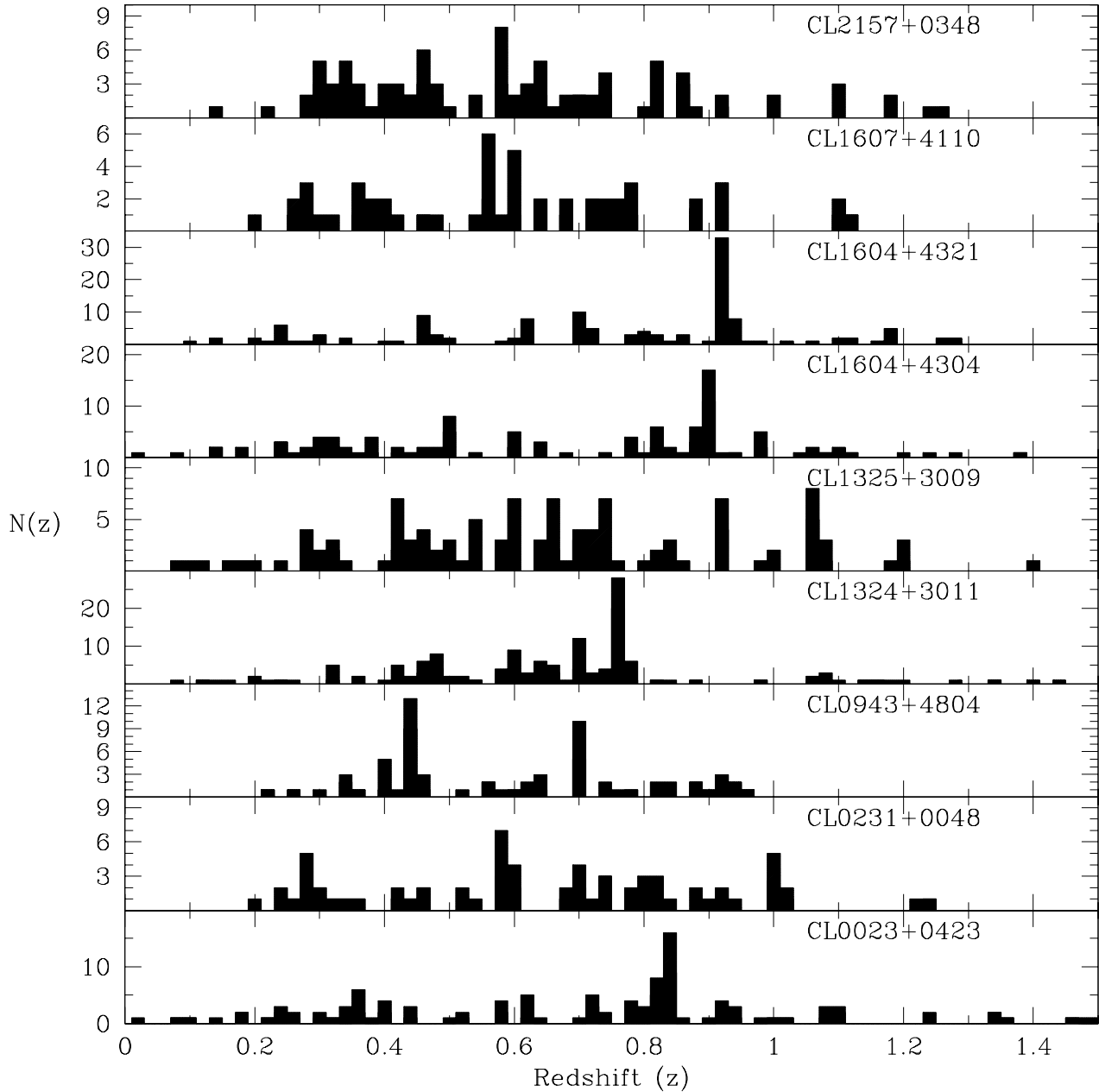


Fig. 3.— The redshift histograms for the nine clusters in this survey.